Influence of Internal Convection during Microwave Thawing of Cylinders

Tanmay Basak and K. G. Ayappa
Dept. of Chemical Engineering, Indian Institute of Science, Bangalore 560012, India

Numerical simulations were carried out for microwave thawing of 2-D cylinders of pure materials with internal convection in the liquid regions. Enthalpy formulation of the energy balance equation was used with a superficial mushy region around the melting point. Electric field, energy and momentum balance equations were solved using the Galerkin finite-element method with the penalty finite-element formulation of the momentum balance equation. Microwave power absorption, temperature, and stream functions were studied for various cases. For samples of diameter D, thawing was contrasted between samples for $0.032 < D/D_p < 3.73$ and $0.10 < D/\lambda_m < 1.58$. These ratios were computed based on the liquid-phase penetration depth D_p and wavelength of microwave radiation in the medium λ_m. In all cases, $Pr = 0.5$ was used and the Rayleigh number varied from 1.067×10^3 for the smallest diameter to 1.33416×10^5 for the largest sample ($D = 2$ cm). Thawing was contrasted for MWs being incident from the top and bottom faces of the cylinder and with the thawing dynamics in the absence of convection in the liquid. Our simulations indicate that convection plays a small role for $D/D_p \ll 1$ and thawing is independent of the direction of MWs. At intermediate values of D/D_p where a strong maximum occurs in the power, the influence of convection with primary and secondary cell formation in the liquid regions was a strong function of the direction of incident microwaves. In the presence of multiple connected thawed regions convection was suppressed.

Introduction

Microwaves (MWs) with their ability to penetrate dielectric materials provide a rapid means of distributing heat source within a sample. During melting or thawing, heating is accompanied by a phase change and the sample can be made up of liquid, solid, and mushy (for multicomponent substances) regions. A successful model for MW thawing hinges on effectively capturing the dynamics of melt formation, which depending on the sample dimension, can occur from any location in the sample due to the penetration of microwaves. The inherent nonlinear and transient nature of the problem is further complicated by the complex shapes of the liquid and solid subdomains that can form during thawing. Due to this, models for MW thawing in the literature which couple the electromagnetics with the heat transport have been primarily restricted to 1-D conduction based models (Pangrle et al., 1991, 1992; Basak and Ayappa, 1997a). We have presented finite-element solutions for MW thawing using a 2-D model for infinite cylinders exposed to plane electromagnetic waves (Basak and Ayappa, 1997b) where we have illustrated the efficacy of the effective heat capacity method, which elegantly captures the dynamics and shapes of liquid, solid, and mushy region formation with a fixed mesh. The primary focus of this article is to incorporate and investigate the effect of liquid convection during melting of a pure material with microwaves.

For a multicomponent material, the transition from solid to liquid occurs via an intermediate state referred to as the mushy region, consisting of co-existing liquid and solid phases where the phase change occurs over a finite temperature range. Unlike pure materials which melt at a distinct temperature, the mushy region prevents the formation of a sharp interface between solid and liquid. Models for phase change

Current address of T. Basak: Dept. of Chemistry, University of Houston, Houston, TX 77204.

in substances which melt over a range of temperatures are known as the effective heat capacity or enthalpy methods (Dalhuijsen and Segal, 1986; Dantzig, 1989). The advantage of these methods is the absence of a front tracking algorithm and are ideally suited to handle multiple thawed regions which arise during MW thawing. A single energy balance is used for the entire domain which may consist of liquid, mush, and solid regions. The occurrence of a particular phase is obtained from the liquid volume fraction vs. temperature relation for the particular material which is an equilibrium relation obtained from the phase diagram of the material. For a pure material, the liquid volume fraction vs. temperature relationship is a step function with the jump occurring at the melting point. In order to incorporate the enthalpy formulation for modeling pure materials we introduce a superficial mushy region around the melting point.

There exists a large literature (Voller and Prakash, 1987; Brent et al., 1988; Dutta et al., 1995) on melting and solidification studies in 2-D rectangular cavities where the phase change is initiated from a wall either maintained at a constant temperature or heated with a constant heat flux. These models are based on the enthalpy-porosity approach for convection-diffusion phase change problems (Voller and Prakash, 1987). In the enthalpy-porosity approach, the enthalpy formulation is coupled with the momentum balance equation due to convective transport and a unified momentum balance equation was developed for flows in porous regions applicable for mushy, as well as liquid, regions. This unified momentum balance approach involves a generation term known as the Darcy term obtained from Darcy's law. The generation term is such that the Navier-Stokes equation is recovered for the liquid region, and the velocities are set to zero in the solid region. The coupled momentum and enthalpy equations were solved using the control volume method (Patankar, 1980). Using the enthalpy-porosity approach, Voller and Prakash (1987) predicted thawing dynamics with the velocity profiles both in liquid, as well as mushy, regions. Brent et al. (1988) carried out melting studies of pure Gallium using the enthalpy-porosity approach and the front positions were in good qualitative agreement with the experimental results of Gau and Viskanta (1986). Dutta et al. (1995) successfully used the enthalpy-porosity approach in moving gas tungsten welding for a 3-D cavity with nonaxisymmetric boundary conditions. Common to all these studies is the absence of volumetric heat generation during the phase change.

A few studies on liquid convection due to volumetric heating effects have been reported in the literature (Gartling, 1982; Datta et al., 1991, 1992; Ayappa et al., 1994; Gilchrist et al., 1998). The study of Gartling (1982) illustrates convection within a rectangular cavity due to a uniform heat source with a maximum temperature occurring in the upper portion of the cavity. Datta et al. (1991, 1992) studied natural convection due to MWs in cylinders assuming that the absorbed microwave power follows a Lambert's law. Ayappa et al. (1994) carried out convection studies in a rectangular cavity due to MWs for various orientations of the incident waves. Maxwell's equations were solved to obtain the absorbed microwave power. Their studies show that when the power peak is located at the bottom of the cavity, convection is the greatest, resulting in uniform temperatures in the sample. Convection was found to play a smaller role where the power peak is situated at the side or top of the wall. Apart from the study by Gilchrist et al. (1998), where the stability of microwave heated fluid layers was examined, we are unaware of any studies on the stability of MW heated 2-D systems. To our knowledge, models which incorporate the effect of liquid convection during MW thawing have not been reported in the literature.

Here we model the MW thawing of a pure substance exposed to uniform plane waves with the focus primarily on the influence of internal convection on the MW thawing characteristics for 2-D cylinders. Transient thawing dynamics are contrasted for MWs incident from the bottom and top of the cylinder. The energy balance equation is based on the enthalpy formulation with convective transport in the liquid. In order to model melting in a pure substance using the enthalpy formulation, a superficial mushy region is assumed around the melting point. The momentum balance is solved in the liquid region alone, and flow in the superficial mushy region is neglected. This is a good approximation, considering the small temperature difference in the superficial mushy region. The coupled electric field, enthalpy and momentum balance equations are solved using the Galerkin finite-element method, with the penalty finite-element formulation used for the momentum balance equation. The advantage of the penalty finite-element method over the conventional pressure-velocity formulation is the elimination of pressure via a penalty parameter. A new feature is the implementation of the radiation boundary condition for the electric field to the half domain problem. Microwave power absorption, temperatures, and stream functions are presented for a range of D/D_p values where D is the sample diameter and D_p is the MW penetration depth within the liquid phase.

Theory

Consider thawing in a 2-D cylinder of radius R, as shown in Figure 1. Plane electromagnetic waves are incident either from the bottom or top, and the cylinder is assumed to be semi-infinite. Initially, the sample is completely frozen at a uniform temperature T_0. The thermal properties in the cylinder are assumed to be isotropic and the surrounding medium is at the temperature T_0 during the entire thawing period. Keeping the surrounding temperature at the initial temperature of the frozen sample minimizes convective heat transfer from the surroundings. In order to use the enthalpy formulation for a pure material a superficial mushy region is assumed. The solids are assumed to be stagnant during thawing and the internal convection is assumed to occur only in the liquid regions. Since the temperature span in the superficial mushy region is small, internal convection in the mushy region is neglected. This assumption is supported by a simple scale analysis given in Appendix A.

Energy and momentum balance equations

For pure materials, such as ice, the liquid volume fraction ϕ_l is a step function of temperature with a discontinuity at the melting point T_m, as shown in Figure 2. To implement the enthalpy method for this situation, we assume a superficial phase change range of ΔT around T_m, within which ϕ_l is

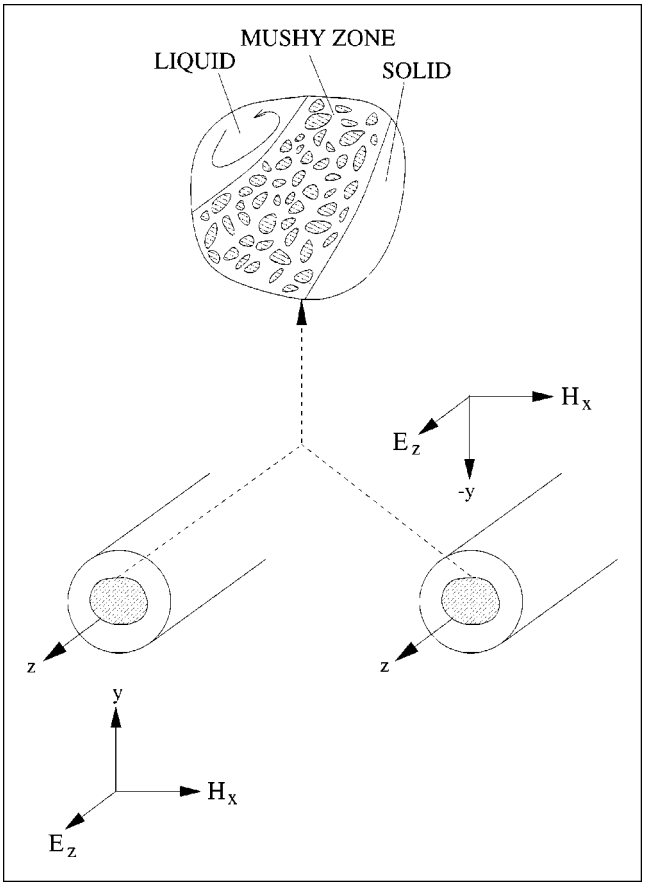

Figure 1. Liquid, solid and mushy regions in a partly thawed sample exposed to a plane electromagnetic wave.

The incident electric field is oriented along the axis (z-axis) of the cylinder. Two incident configurations are shown.

assumed to vary linearly from 0 to 1

$$\phi_l = \begin{cases} 0 & T \le T_i, \\ \dfrac{T - T_i}{(T_f - T_i)} & T_i \le T \le T_f, \\ 1 & T \ge T_f, \end{cases} \quad (1)$$

with $T_i = T_m - \Delta T/2$ and $T_f = T_m + \Delta T/2$. $\Delta T = 0.2$ K was used in all computations. With this assumption, $\phi_l(T)$ reduces to a continuous function removing numerical difficulties associated with a step function. The enthalpy formulation for a domain consisting of solid, liquid, and mushy regions is governed by a single energy balance equation

$$\frac{\partial H}{\partial t} + \delta_l \rho C_l U \cdot \nabla T = \nabla \cdot k_{\text{eff}} \nabla T + q(T), \quad (2)$$

where

$$\delta_l = \begin{cases} 0 & 0 \le \phi_l < 1, \quad \text{solid and mushy} \\ 1 & \phi_l = 1, \quad \text{liquid} \end{cases} \quad (3)$$

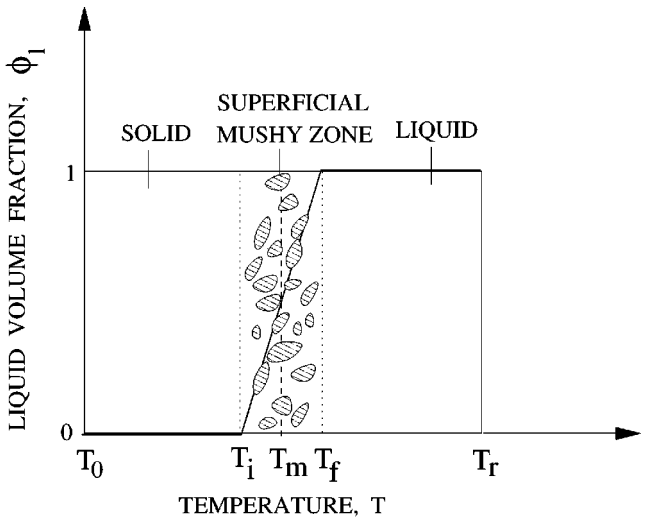

Figure 2. Solid and liquid regions separated by a superficial mushy region.

— — —, The step function for ϕ_l vs. T curve at T_m: —a linear function for ϕ_l vs. T for a superficial mushy region between T_i and T_f. T_0 is the initial temperature of the frozen sample and T_r is the maximum allowable temperature within the sample.

U is the fluid velocity and the enthalpy $H(T)$ which is a function of the temperature at a given location in the sample is

$$H(T) = (1 - \phi_l) \int_{T_0}^{T} \rho C_s(\alpha)\, d\alpha + \phi_l \left[\int_{T_0}^{T_i} \rho C_s(\alpha)\, d\alpha + \rho\lambda + \int_{T_i}^{T} \rho C_t(\alpha)\, d\alpha \right], \quad (4)$$

where C_l and C_s are the heat capacities of the liquid and solid phases, respectively, T_0 is the initial temperature of the frozen sample, and λ is the latent heat of melting. The density ρ of the solid and liquid phases are assumed to be similar. In Eq. 2 the effective thermal conductivity $k_{\text{eff}} = \phi_l k_l + (1 - \phi_l) k_s$, where k_l and k_s are the thermal conductivities of the liquid and solid phases, respectively, and $q(T)$ is the absorbed microwave power. The second term in Eq. 2 represents heat transfer due to internal convection. The associated equation for the momentum transport in the liquid phase given by the Navier-Stokes equation with the Boussinesq approximation for buoyancy driven flow is

$$\rho \frac{\partial U}{\partial t} + \rho U \cdot \nabla U = -\nabla P + \mu \nabla^2 U - \rho_0 \beta (T - T_f) g, \quad (5)$$

and the continuity equation is

$$\nabla \cdot U = 0. \quad (6)$$

In Eq. 5 ρ_0 is the density at the reference temperature T_f, β is the volume expansion coefficient, P is the pressure, and μ is the viscosity. The first two terms in the lefthand side denote the rate of change of momentum and the convective momentum transport, respectively. The first term on the

righthand side denotes momentum transport due to a pressure gradient, the second term is the momentum transport due to viscous forces, and the last term is the momentum transfer due to buoyancy where the density is assumed to vary linearly with temperature. In the Boussinesq approximation, the temperature variation of the fluid density appears only as a body force term (last term in Eq. 5) in the momentum balance equation, and density appearing in the lefthand side of the Eq. 5 is assumed to be a constant (ρ_0).

Using the following dimensionless variables

$$\nabla^* = R\nabla, \quad u = \frac{RU}{\alpha_0}, \quad p = \frac{PR^2}{\rho_0 \alpha_0^2}$$

$$\overline{H} = \frac{H}{\rho_0 C_0 (T_r - T_0)}, \quad \theta = \frac{T - T_0}{T_r - T_0}, \quad \text{and} \quad \tau = \frac{\alpha_0 t}{R^2}. \quad (7)$$

Eqs. 2 and 5 for a 2-D cylinder in dimensionless form are

$$\frac{\partial \overline{H}}{\partial \tau} + \delta_l \overline{\rho C_l} u \cdot \nabla^* \theta = \nabla^* \cdot \left(\overline{k}_{\text{eff}} \nabla^* \theta \right) + Q(\theta), \quad (8)$$

and

$$\frac{\partial u}{\partial \tau} + u \cdot \nabla^* u = -\nabla^* p + Pr \nabla^{*2} u + Ra_m Pr (\theta - \theta_f) e_y. \quad (9)$$

Using Eq. 4, the dimensionless enthalpy $\overline{H}(\theta)$ in Eq. 8 is

$$\overline{H}(\theta) = (1 - \phi_l) \int_{\theta_0}^{\theta} \overline{\rho C_s}(\alpha') d\alpha' + \phi_l \left[\int_{\theta_0}^{\theta_l} \overline{\rho C_s}(\alpha') d\alpha' + \frac{\overline{\rho}}{St_m} + \int_{\theta_l}^{\theta} \overline{\rho C_l}(\alpha') d\alpha' \right]. \quad (10)$$

The dimensionless quantities in Eqs. 8–9 are

$$Q = \frac{qR^2}{k_0 (T_r - T_0)}, \quad \overline{\rho} = \frac{\rho}{\rho_0}, \quad \overline{\rho C_s} = \frac{\rho C_s}{\rho_0 C_0},$$

$$\overline{\rho C_l} = \frac{\rho C_l}{\rho_0 C_0}, \quad \overline{k}_{\text{eff}} = \frac{k_{\text{eff}}}{k_0}, \quad St_m = \frac{C_0 (T_r - T_0)}{\lambda},$$

$$Pr = \frac{\mu}{\rho_0 \alpha_0}, \quad \text{and} \quad Ra_m = \frac{R^3 \rho_0 g \beta (T_r - T_0)}{\mu \alpha_0}.$$

Here ρ_0, C_0, k_0, T_r and α_0 are the reference density, heat capacity, thermal conductivity, reference temperature, and thermal diffusivity, respectively. In Eq. 9, Pr and Ra_m denote the Prandtl number and modified Rayleigh number respectively, and e_y is the vector such that $g = -ge_y$. Typically, the Rayleigh number is a measure of the importance of buoyancy driven flow where flow is driven between a hot and cold plate. In the present situation, where the flow is due to a volumetric heating effect, we defined a modified Rayleigh number Ra_m with respect to the difference between the reference temperature, T_r and the initial temperature T_0. Similarly, St_m in Eq. 10 is the modified Stefan number based on T_r and T_0.

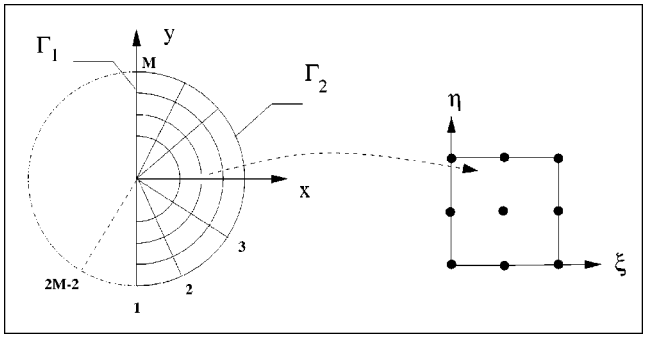

Figure 3. Finite-element mesh used in the study for the cylindrical half domain.

Symmetry conditions for the electric field components and temperature are imposed on Γ_1. Mapping from $x - y$ to $\xi - \eta$ for a representative element is shown.

The reference temperature T_r is typically the maximum allowable temperature within the sample. The initial conditions are

$$\theta(\tau = 0) = 0, \quad \text{and} \quad u(\tau = 0) = 0 \text{ for } -1 \le x, y \le 1. \quad (11)$$

A uniform convective heat-transfer coefficient is maintained at the wall of the cylinder and the fluid velocities satisfy the no slip criteria at the wall. Since the MWs are incident either from the top or bottom, as shown in Figure 1, the heat and the fluid flows are symmetric with respect to the y-axis and solutions are obtained only in the half domain, as shown in Figure 3. The boundary conditions in dimensionless form for the temperature are

$$\frac{\partial \theta}{\partial x} = 0, \quad \text{at} \quad \Gamma_1$$

and

$$-n \cdot \overline{k}_{\text{eff}} \nabla^* \theta = Bi\theta, \quad \text{at} \quad \Gamma_2 \quad (12)$$

where $Bi = hR/k_0$ and h is the heat-transfer coefficient from the sample to the surroundings. For velocities in the liquid region

$$u_x = 0, \quad \frac{\partial u_y}{\partial x} = 0, \quad \text{at} \quad \Gamma_1$$

and

$$u_x = 0, \quad u_y = 0, \quad \text{at} \quad \Gamma_2, \quad (13)$$

where Γ_1 and Γ_2 are the boundaries (see Figure 3). At the interface between the mush and the liquid, the velocity at nodes whose temperature lies in the mushy region are set to zero.

Electric field equations for a cylinder

We consider the microwave thawing in an infinite cylinder where the electric field is oriented along the long axis (z-axis) of the cylinder, as shown in Figure 1. The incident microwave

is a uniform plane wave, with the electric and magnetic components varying in intensity only in the direction of wave propagation (y-axis). In this situation Maxwell's equations for the electric field E_z reduce to a single equation

$$\nabla^2 E_z + k^2(\phi_l) E_z = 0, \tag{14}$$

where ϕ_l is the liquid volume fraction and the propagation constant

$$k = \frac{\omega}{c}\sqrt{\kappa'(\phi_l) + i\kappa''(\phi_l)}, \tag{15}$$

depends on $\kappa'(\phi_l)$, the relative dielectric constant and $\kappa''(\phi_l)$, the relative dielectric loss. The dielectric constant measures the ability to store electric energy and the dielectric loss measures the ability to convert electric energy into heat. Here $\omega = 2\pi f$, where f is the frequency of the electromagnetic wave and c is the velocity of light. We assume that the dielectric properties are temperature-dependent only due to their dependence on ϕ_l. Hence, in regions of pure liquid and solid the dielectric properties are assumed to be independent of temperature. Previous studies on the influence of temperature-dependent dielectric properties indicate that this is a good assumption at 2,450 MHz (Ayappa et al., 1991). The dielectric properties in the superficial mushy region are the functions of the dependent liquid volume fraction, and the mixture rules for κ' and κ'' are similar to those used in our earlier work (Basak and Ayappa, 1997a).

The power absorbed per unit volume is

$$q = \frac{1}{2}\omega\epsilon_0\kappa'' E_z E_z^*, \tag{16}$$

where ϵ_0 is the free space permittivity and E_z^* is the complex conjugate of E_z. For a given flux of incident radiation I_0 in free space the incident electric field intensity E_0 is given by

$$E_0 = \sqrt{\frac{2I_0}{c\epsilon_0}} \tag{17}$$

It is assumed in the model that the liquid and solid phases are always separated by a mushy region (Figure 2) which is found to be true for all the cases simulated here. This coupled with the continuity of the ϕ_l vs. T relationship always ensures that the dielectric properties are continuous across the sample. Hence, interface conditions between solid and mush or liquid and mush are not required while solving the electric field equation.

Using the dimensionless variables

$$u_z = \frac{E_z}{E_0} \quad \text{and} \quad \nabla^* = R\nabla,$$

Equation 14 reduces to

$$\nabla^{*2} u_z + \gamma^2(\phi_l) u_z = 0, \tag{18}$$

where u_z is the electric field intensity and $\gamma(\phi_l) = (R\omega/c)\sqrt{\kappa'(\phi_l) + i\kappa''(\phi_l)}$ is the propagation constant. Substituting the complex field variable $u_z = v_z + iw_z$ into Eq. 18 and equating the real and imaginary components

$$\nabla^{*2} v_z + \chi_1(\phi_l) v_z - \chi_2(\phi_l) w_z = 0 \tag{19}$$

and

$$\nabla^{*2} w_z + \chi_2(\phi_l) v_z + \chi_1(\phi_l) w_z = 0, \tag{20}$$

where $\chi_1(\phi_l) = (R^2\omega^2/c^2)\kappa'(\phi_l)$ and $\chi_2(\phi_l) = (R^2\omega^2/c^2)\kappa''(\phi_l)$.

A radiation boundary condition (RBC) is used to prevent calculating the electric field exterior to the sample. Since the dielectric properties external to the cylinder are invariant, the field outside the cylinder can be expressed using a series solution. Using the Dirchlet to Neumann mapping, an RBC that can be applied at the surface of the cylinder is obtained. The details of the derivation are given by Ayappa et al. (1992). In this article we illustrate how the RBC can be applied to the half-domain, the details of which are given in Appendix B. The RBCs for v_z and w_z are

$$\begin{aligned} n\cdot\nabla^* v_z = &\sum_{n=0}^{\infty} Re(C_n)\cos n\phi \\ &+ \sum_{n=0}^{\infty} Re(D_n)\int_0^{2\pi} v_z(1,\phi')\cos n(\phi-\phi')\,d\phi' \\ &- \sum_{n=0}^{\infty} Im(D_n)\int_0^{2\pi} w_z(1,\phi')\cos n(\phi-\phi')\,d\phi' \end{aligned} \tag{21}$$

and

$$\begin{aligned} n\cdot\nabla^* w_z = &\sum_{n=0}^{\infty} Im(C_n)\cos n\phi \\ &+ \sum_{n=0}^{\infty} Im(D_n)\int_0^{2\pi} v_z(1,\phi')\cos n(\phi-\phi')\,d\phi' \\ &+ \sum_{n=0}^{\infty} Re(D_n)\int_0^{2\pi} w_z(1,\phi')\cos n(\phi-\phi')\,d\phi' \end{aligned} \tag{22}$$

where the coefficients

$$C_n = \epsilon_n i^n \omega^* \left[J_n'(\omega^*) - J_n(\omega^*)\frac{H_n^{(1)'}(\omega^*)}{H_n^{(1)}(\omega^*)} \right] \tag{23}$$

and

$$D_n = \frac{\omega^* \delta_n H_n^{(1)'}(\omega^*)}{\pi H_n^{(1)}(\omega^*)} \tag{24}$$

and

$$\epsilon_n = \begin{cases} 1, & n = 0; \\ 2, & \text{otherwise}, \end{cases} \quad \text{and} \quad \delta_n = \begin{cases} 1/2, & n = 0; \\ 1, & \text{otherwise}. \end{cases} \tag{25}$$

In the above equations $\omega^* = \omega R/c$, J_n and $H_n^{(1)}$ are the Bessel and Hankel functions of the first kind, respectively, and the prime indicates the first derivatives (Abramowitz and Stegun, 1970). The expression for the microwave power term in Eq. 8 is

$$Q[\phi_l(\theta)] = \frac{R^2\omega\epsilon_0\kappa''(\phi_l)E_0^2}{2k_0(T_r - T_0)}(v_z^2 + w_z^2) \tag{26}$$

Microwave power absorption: characteristic parameters

Using the relationship between the dielectric constants with λ_m and D_p (Ayappa, 1997) the propagation constant in Eq. 14 can be expressed as

$$k = (2\pi/\lambda_m) + i(1/D_p). \tag{27}$$

The above form of the propagation constant indicates that for a fixed incident frequency and intensity, λ_m and D_p are the two length scales that determine the electric field distribution in the sample. The material dielectric loss κ'' in terms of D_p and λ_m, obtained from Eqs. 15 and 27 by equating real and imaginary parts, is

$$\kappa'' = \frac{4\pi c^2}{\omega^2\lambda_m D_p}. \tag{28}$$

Using Eqs. 17 and 28, the microwave power term (Eq. 26) reduces to

$$Q = \left(\frac{D}{D_p}\right)\left(\frac{D}{\lambda_m}\right)G(v_z^2 + w_z^2), \tag{29}$$

where $D = 2R$ is the sample diameter, $G = \lambda_0 I_0/2k_0(T_r - T_0)$, and $\lambda_0 = c/f$ is the wavelength of radiation in free space. The electric field distributions (v_z, w_z) are functions of the sample dimension; hence, for a constant D, the three parameters D/D_p, D/λ_m and G are the natural dimensionless numbers for the MW heating. Since the dielectric properties vary spatially within the mushy region, a constant value for D_p and λ_m cannot be obtained during thawing. In the present study, we choose D_p and λ_m for the liquid phase as appropriate length scales, since the microwave power absorption in the solid phase is very small.

Solution procedure

The energy balance equation Eq. 8, momentum balance for the liquid region Eq. 9, and the electric field equations Eqs. 19 and 20 are solved using the Galerkin finite-element method. In order to solve Eq. 9, we use the penalty finite-element method where the pressure p is eliminated via a penalty parameter γ with the incompressibility condition ($\nabla^* \cdot u = 0$) treated as a constraint. The penalty finite-element method is a standard technique for solving incompressible viscous flows, and there exists a larger literature on the subject (Hughes et al., 1979; Reddy, 1993, others). In order to implement the penalty finite-element formulation the pressure expressed in terms of the penalty parameter and the continuity equation is

$$p = -\gamma(\nabla^* \cdot u) \tag{30}$$

As a consequence, the continuity equation is satisfied in the limit of large γ. Numerical tests indicate that typical values of γ that yield consistent solutions are 10^7 (Reddy, 1993). Using Eq. 30, the momentum balance equation (Eq. 9) is

$$\frac{\partial u}{\partial \tau} + u\cdot\nabla^* u = \gamma\nabla^*(\nabla^*\cdot u) + Pr\nabla^{*2}u + Ra_m Pr(\theta - \theta_f)e_y. \tag{31}$$

The velocity components (u_x and u_y) obtained from Eq. 31 are

$$\frac{\partial u_x}{\partial \tau} + u_x\frac{\partial u_x}{\partial x} + u_y\frac{\partial u_x}{\partial y} = \gamma\frac{\partial}{\partial x}\left(\frac{\partial u_x}{\partial x} + \frac{\partial u_y}{\partial y}\right) + Pr\left(\frac{\partial^2 u_x}{\partial x^2} + \frac{\partial^2 u_x}{\partial y^2}\right), \tag{32}$$

and

$$\frac{\partial u_y}{\partial \tau} + u_x\frac{\partial u_y}{\partial x} + u_y\frac{\partial u_y}{\partial y} = \gamma\frac{\partial}{\partial y}\left(\frac{\partial u_x}{\partial x} + \frac{\partial u_y}{\partial y}\right) + Pr\left(\frac{\partial^2 u_y}{\partial x^2} + \frac{\partial^2 u_y}{\partial y^2}\right) + Ra_m Pr(\theta - \theta_f). \tag{33}$$

The symmetry of the microwave radiation with respect to $x = 0$, as shown in Figure 1, results in a temperature distribution which is also symmetric with respect to $x = 0$ for both the bottom and top incident microwave radiations. Hence, we solve the equations only in one-half of the cylinder, as shown in Figure 3. Expanding the real (v_z) and imaginary components (w_z) of the electric field, the temperature (θ) and the velocity components (u_x, u_y) in a basis set $\{\Phi\}$

$$v_z \approx \sum_{k=1}^{N} v_{z,k}\Phi_k(x,y), \quad w_z \approx \sum_{k=1}^{N} w_{z,k}\Phi_k(x,y), \quad \theta \approx \sum_{k=1}^{N} \theta_k\Phi_k(x,y), \quad u_x \approx \sum_{k=1}^{N} u_{x,k}\Phi_k(x,y), \quad \text{and} \quad u_y \approx \sum_{k=1}^{N} u_{y,k}\Phi_k(x,y), \tag{34}$$

for

$$-1 \le x, y \le 1,$$

the Galerkin finite-element method yields the following nonlinear residual equations for Eqs. 19 and 20, 8, 32, and 33, respectively

$$R_i^{(1)} = \sum_{k=1}^{N} v_{z,k}^{t+1}\int_\Omega\left[\frac{\partial\Phi_i}{\partial x}\frac{\partial\Phi_k}{\partial x} + \frac{\partial\Phi_i}{\partial y}\frac{\partial\Phi_k}{\partial y}\right]dxdy + \sum_{k=1}^{N} w_{z,k}^{t+1}\int_\Omega\chi_2(\phi_l^{t+1})\Phi_i\Phi_k\,dxdy - \sum_{k=1}^{N} v_{z,k}^{t+1}\int_\Omega\chi_1(\phi_l^{t+1})\Phi_i\Phi_k\,dxdy - \int_{\Gamma_2}\Phi_i n\cdot\nabla^* v_z^{t+1}d\Gamma \tag{35}$$

$$R_i^{(2)} = \sum_{k=1}^{N} w_{z,k}^{t+1} \int_\Omega \left[\frac{\partial \Phi_i}{\partial x} \frac{\partial \Phi_k}{\partial x} + \frac{\partial \Phi_i}{\partial y} \frac{\partial \Phi_k}{\partial y} \right] dxdy$$

$$- \sum_{k=1}^{N} v_{z,k}^{t+1} \int_\Omega \chi_2\left(\phi_l^{t+1}\right) \Phi_i \Phi_k \, dxdy$$

$$- \sum_{k=1}^{N} w_{z,k}^{t+1} \int_\Omega \chi_1\left(\phi_l^{t+1}\right) \Phi_i \Phi_k \, dxdy - \int_{\Gamma_2} \Phi_i n \cdot \nabla^* w_z^{t+1} d\Gamma \quad (36)$$

$$R_i^{(3)} = \sum_{k=1}^{N} \int_\Omega \left\{ \frac{\overline{H}_k^{t+1} - \overline{H}_k^t}{\Delta\tau} \right\} \Phi_i \Phi_k \, dxdy$$

$$+ \frac{1}{2} \left[F_1\left(v_z^{t+1}, w_z^{t+1}, \theta^{t+1}, u_x^{t+1}, u_y^{t+1}, \phi_l^{t+1}\right) \right.$$

$$\left. + F_1\left(v_z^t, w_z^t, \theta^t, u_x^t, u_y^t, \phi_l^t\right) \right] \quad (37)$$

$$R_i^{(4)} = \sum_{k=1}^{N} \int_\Omega \left\{ \frac{u_{x,k}^{t+1} - u_{x,k}^t}{\Delta\tau} \right\} \Phi_i \Phi_k \, dxdy$$

$$+ \frac{1}{2} \left[F_2\left(\theta^{t+1}, u_x^{t+1}, u_y^{t+1}, \phi_l^{t+1}\right) + F_2\left(\theta^t, u_x^t, u_y^t, \phi_l^t\right) \right] \quad (38)$$

$$R_i^{(5)} = \sum_{k=1}^{N} \int_\Omega \left\{ \frac{u_{y,k}^{t+1} - u_{y,k}^t}{\Delta\tau} \right\} \Phi_i \Phi_k \, dxdy$$

$$+ \frac{1}{2} \left[F_3\left(\theta^{t+1}, u_x^{t+1}, u_y^{t+1}, \phi_l^{t+1}\right) + F_3\left(\theta^t, u_x^t, u_y^t, \phi_l^t\right) \right] \quad (39)$$

where $\overline{H}_k^t$ is evaluated using Eq. 10 as

$$\overline{H}_k^t = (1 - \phi_l)\overline{\rho C_s} \sum_{k=1}^{N} \theta_k^t \Phi_k$$

$$+ \phi_l \left[\overline{\rho C_s} \theta_i + \frac{\overline{\rho}}{St_m} + \overline{\rho C_l} \left(\sum_{k=1}^{N} \theta_k^t \Phi_k - \theta_i \right) \right], \quad (40)$$

$$F_1\left(v_z^t, w_z^t, \theta^t, u_x^t, u_y^t, \phi_l^t\right)$$

$$= \delta_l \overline{\rho C_l} \sum_{k=1}^{N} \theta_k^t \int_\Omega \left[\left(\sum_{k=1}^{N} u_{x,k}^t \Phi_k \right) \frac{\partial \Phi_k}{\partial x} \right.$$

$$\left. + \left(\sum_{k=1}^{N} u_{y,k}^t \Phi_k \right) \frac{\partial \Phi_k}{\partial y} \right] \Phi_i \, dxdy$$

$$+ \sum_{k=1}^{N} \theta_k^t \int_\Omega \overline{k}_{\text{eff}}\left(\phi_l^t\right) \left[\frac{\partial \Phi_i}{\partial x} \frac{\partial \Phi_k}{\partial x} + \frac{\partial \Phi_i}{\partial y} \frac{\partial \Phi_k}{\partial y} \right] dxdy$$

$$- \frac{R^2 \omega \epsilon_0 E_0^2}{2 k_0 (T_r - T_0)} \int_\Omega \kappa''\left(\phi_l^t\right) \left\{ \left(\sum_{k=1}^{N} v_{z,k}^t \Phi_k \right)^2 \right.$$

$$\left. + \left(\sum_{k=1}^{N} w_{z,k}^t \Phi_k \right)^2 \right\} \Phi_i \, dxdy + \int_{\Gamma_2} \Phi_i Bi \theta^{t+1} d\Gamma \quad (41)$$

$$F_2\left(\theta^t, u_x^t, u_y^t, \phi_l^t\right) = \sum_{k=1}^{N} u_{x,k}^t \int_\Omega \left[\left(\sum_{k=1}^{N} u_{x,k}^t \Phi_k \right) \frac{\partial \Phi_k}{\partial x} \right.$$

$$\left. + \left(\sum_{k=1}^{N} u_{y,k}^t \Phi_k \right) \frac{\partial \Phi_k}{\partial y} \right] \Phi_i \, dxdy$$

$$+ \gamma \left[\sum_{k=1}^{N} u_{x,k}^t \int_\Omega \frac{\partial \Phi_i}{\partial x} \frac{\partial \Phi_k}{\partial x} dxdy + \sum_{k=1}^{N} u_{y,k}^t \int_\Omega \frac{\partial \Phi_i}{\partial x} \frac{\partial \Phi_k}{\partial y} dxdy \right]$$

$$+ Pr \sum_{k=1}^{N} u_{x,k}^t \int_\Omega \left[\frac{\partial \Phi_i}{\partial x} \frac{\partial \Phi_k}{\partial x} + \frac{\partial \Phi_i}{\partial y} \frac{\partial \Phi_k}{\partial y} \right] dxdy$$

$$- Pr \int_{\Gamma_1} n \cdot \nabla u_x^t \Phi_i d\Gamma \quad (42)$$

$$F_3\left(\theta^t, u_x^t, u_y^t, \phi_l^t\right) = \sum_{k\text{-}1}^{N} u_{y,k}^t \int_\Omega \left[\left(\sum_{k=1}^{N} u_{x,k}^t \Phi_k \right) \frac{\partial \Phi_k}{\partial x} \right.$$

$$\left. + \left(\sum_{k=1}^{N} u_{y,k}^t \Phi_k \right) \frac{\partial \Phi_k}{\partial y} \right] \Phi_i \, dxdy + \gamma \left[\sum_{k=1}^{N} u_{x,k}^t \right.$$

$$\left. \int_\Omega \frac{\partial \Phi_i}{\partial y} \frac{\partial \Phi_k}{\partial x} dxdy + \sum_{k=1}^{N} u_{y,k}^t \int_\Omega \frac{\partial \Phi_i}{\partial y} \frac{\partial \Phi_k}{\partial y} dxdy \right]$$

$$+ Pr \sum_{k=1}^{N} u_{y,k}^t \int_\Omega \left[\frac{\partial \Phi_i}{\partial x} \frac{\partial \Phi_k}{\partial x} + \frac{\partial \Phi_i}{\partial y} \frac{\partial \Phi_k}{\partial y} \right] dxdy$$

$$- Ra_m Pr \int_\Omega \left[\left(\sum_{k=1}^{N} \theta_k^t \Phi_k \right) - \theta_f \right] \Phi_i \, dxdy$$

$$- Pr \int_{\Gamma_1} n \cdot \nabla u_y^t \Phi_i d\Gamma \quad (43)$$

and

$$i = 1 \ldots N \text{ and } t = \text{time index}$$

The gradients of the electric field in the surface integrals due to RBC of Eqs. 35 and 36 are evaluated for a half domain (see Figure 3). The unconditionally stable Crank-Nicholson algorithm is used to discretize the time domain in Eqs. 37–39 and biquadratic basis functions with three point Gaussian quadrature are used to evaluate the integrals in the residual equations.

In Eqs. 42 and 43 the second integral containing the penalty parameter (γ) are evaluated with two point Gaussian quadrature (reduced integration penalty formulation, Reddy, 1993; Hughes, 1979). It has been found that lowering the order of integration is necessary to prevent ill-conditioning of the Jacobian for large values of γ. The nonlinear residual equations (Eqs. 35–39) are solved using a Newton-Raphson procedure to determine the coefficients of the expansions in Eq. 34 at each time step. At each time step, the linear ($5N \times 5N$) system solved is

$$J\left(a^{n,t+1}\right)\left[a^{n,t+1} - a^{n+1,t+1}\right] = R\left(a^{n,t+1}\right), \quad (44)$$

where n is the Newton iterate index and t the time index. The elements of the Jacobian matrix, $J(a^{n,t+1})$ contains the derivatives of the residual equations with respect to the temperature (θ's), velocity vectors (u_x)'s, (u_y)'s electric field unknowns (v_z's) and w_z's) and $R(a^{n,t+1})$ is the vector of residuals. The fluid motion is displayed via the stream function ψ obtained from velocity u_x and u_y.

Domain discretizations and integrations

Finite-element meshes for the computational domain are shown in Figure 3. Mesh numbering from the center outward was used in both cases. We have used nine node biquadratic elements with each element mapped using isoparametric mapping (Reddy, 1993) from $x-y$ to a unit square $\xi-\eta$ domain, as shown in Figure 3. Correspondingly, the domain integrals in the residual equations are evaluated using nine node biquadratic basis functions in $\xi-\eta$ domain using

$$x=\sum_{i=1}^{9} x_i\Phi_i(\xi,\eta) \quad \text{and} \quad y=\sum_{i=1}^{9} y_i\Phi_i(\xi,\eta), \qquad (45)$$

where $\Phi_i(\xi,\eta)$ are the local biquadratic basis functions on the $\xi-\eta$ domain. At the center of the cylinder, collapsed elements are used where three nodes share the co-ordinates at the origin.

RBC for the half domain

With the finite-element expansions in Eq. 34 and RBCs from Eqs. 21 and 22, the boundary integrals for M nodes on Γ_2 (Figure 3) are

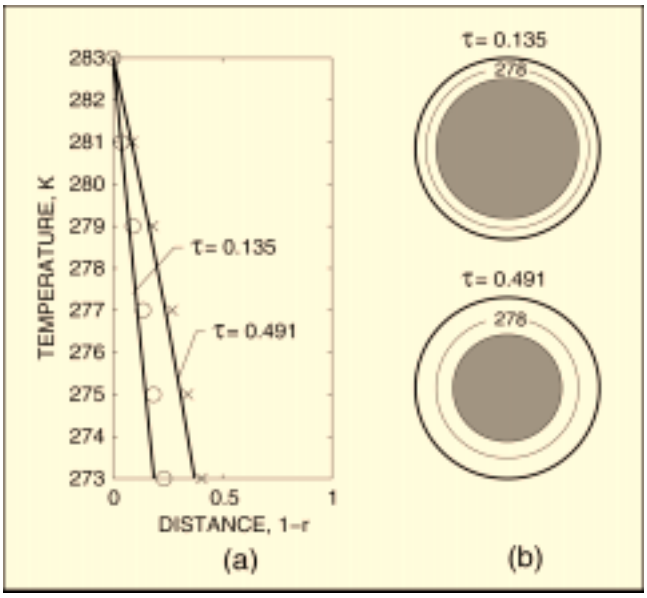

Figure 4. (a) Comparison of temperature distributions: — solution obtained by modified isotherm migration method (Talmon et al., 1983) and ○, × finite-element solution; (b) temperature contours obtained by the finite-element solution. The shaded region denotes the solid phase. The distance $1-r$ is measured from the outer surface of the cylinder.

$$\int_{\Gamma_2}\Phi_i n\cdot\nabla^* v_z\,d\Gamma=\sum_{n}^{\infty} Re(C_n)\xi_{\text{in}}^h + \sum_{j=1}^{M} v_j\sum_{n=0}^{\infty} Re(D_n)\Big[\xi_{\text{in}}^h\big(\xi_{j,n}^f+\beta_{1j}\beta_{Mj}\xi_{2M-j,n}^f\big) + \eta_{\text{in}}^h\big(\eta_{j,n}^f+\beta_{1j}\beta_{Mj}\eta_{2M-j,n}^f\big)\Big] - \sum_{j=1}^{M} w_j\sum_{n=0}^{\infty} Im(D_n)\Big[\xi_{in}^h\big(\xi_{j,n}^f+\beta_{1j}\beta_{Mj}\xi_{2M-j,n}^f\big) + \eta_{\text{in}}^h\big(\eta_{j,n}^f+\beta_{1j}\beta_{Mj}\eta_{2M-j,n}^f\big)\Big], \qquad (46)$$

and

$$\int_{\Gamma_2}\Phi_i n\cdot\nabla^* w_z\,d\Gamma=\sum_{n}^{\infty} Im(C_n)\xi_{\text{in}}^h + \sum_{j=1}^{M} v_j\sum_{n=0}^{\infty} Im(D_n)\Big[\xi_{\text{in}}^h\big(\xi_{j,n}^f+\beta_{1j}\beta_{Mj}\xi_{2M-j,n}^f\big) + \eta_{\text{in}}^h\big(\eta_{j,n}^f+\beta_{1j}\beta_{Mj}\eta_{2M-j,n}^f\big)\Big] + \sum_{j=1}^{M} w_j\sum_{n=0}^{\infty} Re(D_n)\Big[\xi_{\text{in}}^h\big(\xi_{j,n}^f+\beta_{1j}\beta_{Mj}\xi_{2M-j,n}^f\big) + \eta_{\text{in}}^h\big(\eta_{j,n}^f+\beta_{1j}\beta_{Mj}\eta_{2M-j,n}^f\big)\Big], \qquad (47)$$

where

$$\left.\begin{aligned}\xi_{ln}^h&=\int_0^{\pi}\cos n\alpha\,\Phi_\ell\,d\alpha, \quad \xi_{ln}^f=\int_0^{2\pi}\cos n\alpha\,\Phi_\ell\,d\alpha\\ \eta_{ln}^h&=\int_0^{\pi}\sin n\alpha\,\Phi_\ell\,d\alpha, \quad \eta_{ln}^f=\int_0^{2\pi}\sin n\alpha\,\Phi_\ell\,d\alpha\end{aligned}\right\} l=i,j. \qquad (48)$$

and $\beta_{ij}=1-\delta_{ij}$, where δ_{ij} is the Kronecker delta symbol, with the property

$$\delta_{ij}=\begin{cases}0, & i\neq j;\\ 1, & i=j,\end{cases} \qquad (49)$$

The summations over the index n refer to the coefficients involving Bessel functions, typically, $M=15$ to 20. Note that the RBC involves integrals for the full domain, as well as for the half domain. The full domain ($0<\phi<2\pi$) integrals arise during the derivation of the RBC and are a consequence of the orthogonality relationships (Ayappa et al., 1992). The half domain integrals ($0<\phi<\pi$) are due to the restriction of the finite-element solution to the half domain Γ_2. The details of the derivation and implementation for one representative term in the RBC are outlined in Appendix B.

Evaluation of stream function

The relationships between stream function ψ (Batchelor, 1993) and velocity vectors for 2-D flows are

$$u_x=\frac{\partial\psi}{\partial y}, \quad u_y=-\frac{\partial\psi}{\partial x}, \qquad (50)$$

which yield a single equation

$$\nabla^2\psi = \frac{\partial u_x}{\partial y} - \frac{\partial u_y}{\partial x}. \quad (51)$$

Using the above definition of the stream function (Batchelor, 1993), the positive sign of ψ denotes anticlockwise circulation and the clockwise circulation can be represented by the negative sign of ψ. Expanding the stream function (ψ) in a basis set $\{\Phi\}$ as $\psi = \sum_{k=1}^{N} \psi_k \Phi_k(x, y)$ and using the relation for u_x and u_y from Eq. 34, the Galerkin finite-element yield the following linear residual equations for Eq. 51

$$R_i^s = \sum_{k=1}^{N} \psi_k^{t+1} \int_\Omega \left[\frac{\partial \Phi_i}{\partial x}\frac{\partial \Phi_k}{\partial x} + \frac{\partial \Phi_i}{\partial y}\frac{\partial \Phi_k}{\partial y} \right] dxdy + \sum_{k=1}^{n} u_{x,k}^{t+1} \int_\Omega \Phi_i \frac{\partial \Phi_k}{\partial y} dxdy - \sum_{k=1}^{n} u_{y,k}^{t+1} \int_\Omega \Phi_i \frac{\partial \Phi_k}{\partial x} dxdy - \int_{\Gamma_2} \Phi_i n \cdot \nabla^* \psi^{t+1} d\Gamma \quad (52)$$

The no-slip condition is valid at Γ_2 (Figure 3) and there is no cross flow along Γ_1 (Figure 3), hence $\psi = 0$ is used for nodes at Γ_1 and Γ_2. The biquadratic basis function is used to evaluate the integrals in Eq. 52 and ψ's are obtained by solving the N linear residual equations (Eq. 52).

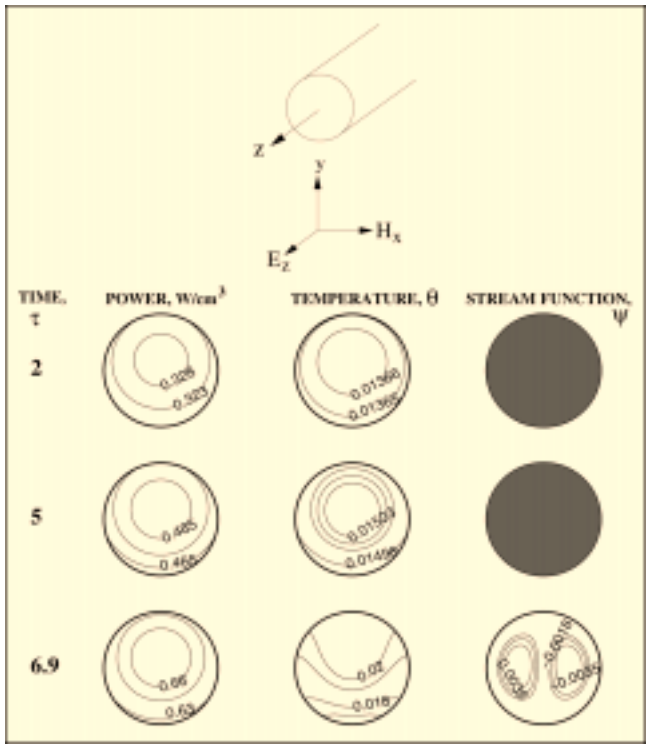

Figure 5. Power, temperature and stream function contours during microwave thawing for a $D = 0.4$ cm cylinder exposed to microwaves from the bottom.

$D/D_p = 0.032$, $D/\lambda_m = 0.104$, $Pr = 0.5$, $Ra_m = 1.067 \times 10^3$, $G = 9$, $St_m = 6.8$, $Bi = 0.004$. Circulations occur when the sample is completely thawed.

Results

Numerical tests

Prior to discussing our results on microwave thawing, we report the various tests that were carried out. Figure 4 illustrates the thawing of a pure material with the enthalpy formulation in the absence of convection and without MWs, with a superficial mushy region of width $\Delta T = 0.2$ K. Here, the boundary of the cylinder was maintained at a constant temperature of 283 K and the solid region which is at an initial temperature of 273 K is retained at this temperature during the process. The temperature variation in the liquid region and the isotherms are shown in the Figures 4a and 4b, respectively. We have compared the temperatures with the data taken from Talmon et al. (1983) where a modified isotherm migration method was used. We note that while using the enthalpy formulation with the superficial mushy region, the thermal properties of the solid phase are required (Eq. 4). Since this data are not available, the thermal properties of the solid were assumed to be that of the liquid. Figure 4b illustrates that the melting front is clearly resolved.

To test the penalty finite-element method we solved the 2-D flow in a driven cavity problem. Computations were carried out for $Re = 400$ and 1,000 and compared with the results of Schreiber and Keller (1983). In all cases the agreement was excellent. We studied the effect of varying the penalty parameter γ for two different Reynolds numbers. Based on these tests, $\gamma = 10^7$ was used in all our simulations. Tests for buoyancy driven convection in the absence of MWs

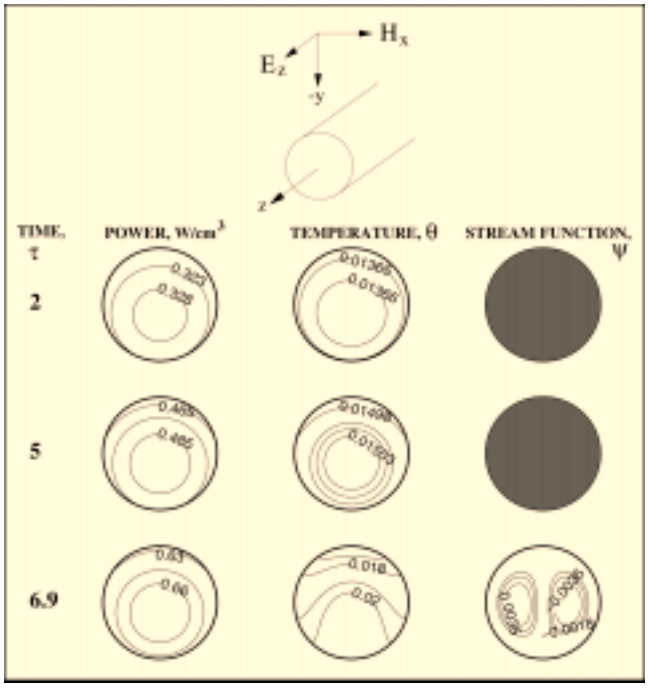

Figure 6. Same parameters as in Figure 5, but MWs are incident from the top.

were carried out for liquid in a cavity with Dirichlet boundary conditions on the side walls and insulated bottom and top walls (Mallinson and Davis, 1977), and for fluid being heated between a hotter inner cylinder and a cooler outer cylinder (Kuehn and Goldstein, 1976).

Microwave thawing

In order to study the effect of changing dielectric and thermal properties on MW thawing, computations were carried out in the following manner. The solid phase λ_m and D_p were held constant by fixing the dielectric properties of the solid phase $\kappa_s' = 5$, $\kappa_s'' = 0.5$. For a fixed sample diameter D, the dielectric properties of the liquid phase were varied to investigate heating patterns in samples with different D/D_p and D/λ_m ratios. The relevant dimensionless numbers are mentioned below each figure. The D/D_p and D/λ_m values reported and mentioned in the discussion below are based on the liquid phase D_p and λ_m. In all cases the incident frequency $f = 2{,}450$ MHz and the intensity of incident radiation $I_0 = 1$ W·cm^{-2}. The temperature and time are reported in dimensionless units, and, for all simulations, the melting point is assumed to be 273 K with a superficial mushy region of width $\Delta T = 0.2$ K. The number of elements in the finite-element solution vary between 10×10 to 14×14 for 0.4 cm $< D \leq 1$ cm, and, for $D = 2$, cm 16×16 elements were used. Typical time steps were $\Delta\tau = 10^{-3}$–10^{-5} and smaller times steps were required for strong circulations. We have used constant thermal properties in the solid and liquid phases, that is, $C_l = C_s = C_0$, $k_l = k_s = k_0$. The computations were carried out in IBM 590 workstations and the typical CPU time varied from 16 h for the smaller cylinders to about 140 h for the larger cylinder.

Figure 5 illustrates the power, temperature and stream functions at different time intervals for a small sample ($D =$ 0.4 cm) heated with microwaves from below. The shaded region in the plots represent the mushy (''solid') region where 272.9 K $< T <$ 273.1 K. Since $D/D_p = 0.032$, the power absorption and temperatures are uniform across the sample and the entire sample turns mushy during heating. At $\tau = 6.9$, the sample is completely thawed and two circulation cells, which extend across the sample, are observed.

The results in Figure 6 are for the same conditions as in Figure 5, except the MWs are now incident from the top of the sample. For comparison, the different stages are shown at the same time intervals for the bottom incidence case in Figure 5. Due to the uniform power absorption, the direction of the incident wave is seen to have little influence on the thawing dynamics. In Figure 7 the sample diameter is increased to $D = 1$ cm, $D/D_p = 0.18$. For MWs incident from the bottom (Figure 7), the maximum power absorption occurs at the top of the sample and the liquid region forms initially in the upper portions of the cylinder. Two circulation cells form in the liquid region, which grow in size as thawing proceeds, and, when thawing is complete, four cells are formed. This is due to a local minimum in the absorbed power formed

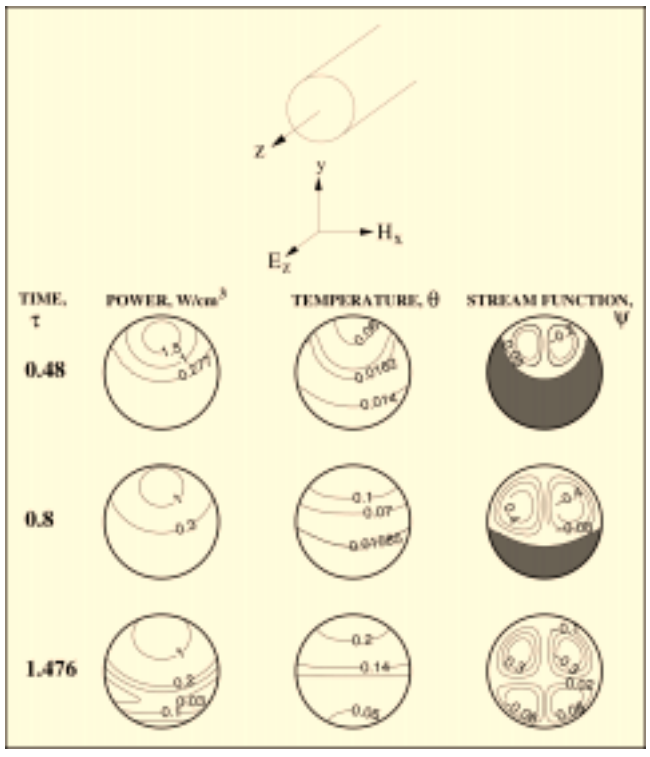

Figure 7. Power, temperature and stream function contours during microwave thawing for a $D = 1$ cm cylinder exposed to microwaves from the bottom.

$D/D_p = 0.18$, $D/\lambda_m = 0.58$, $Pr = 0.5$, $Ra_m = 1.6677 \times 10^4$, $G = 9$, $St_m = 6.8$, $Bi = 0.01$. Four convection cells occur when the sample is completely thawed.

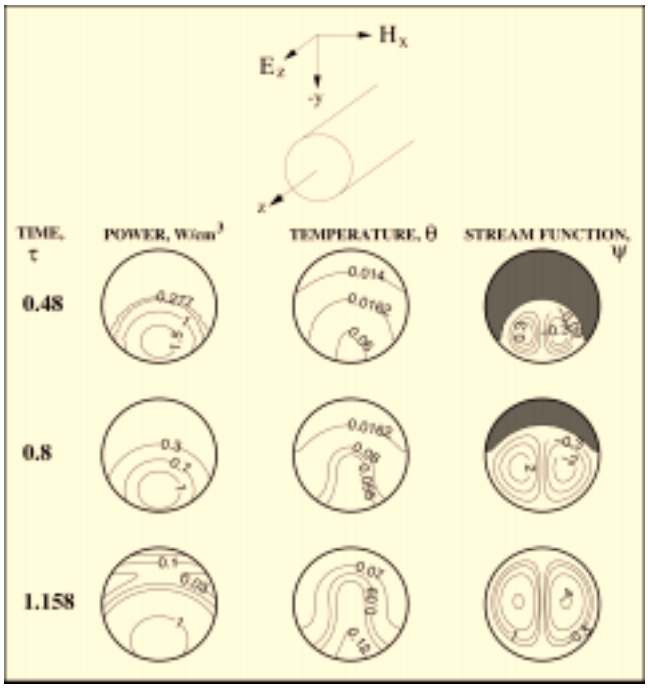

Figure 8. Same parameters as in Figure 7, but MWs are incident from the top.

Greater convection results in uniform temperature distribution within the sample.

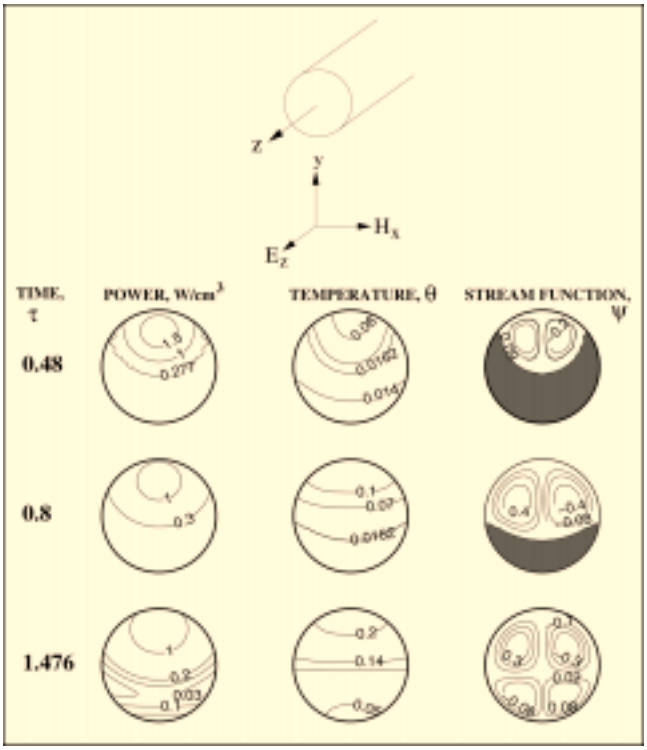

Figure 9. Parameters similar to that of Figure 7 when 12×12 elements are used.

Results are shown for 10×10 elements.

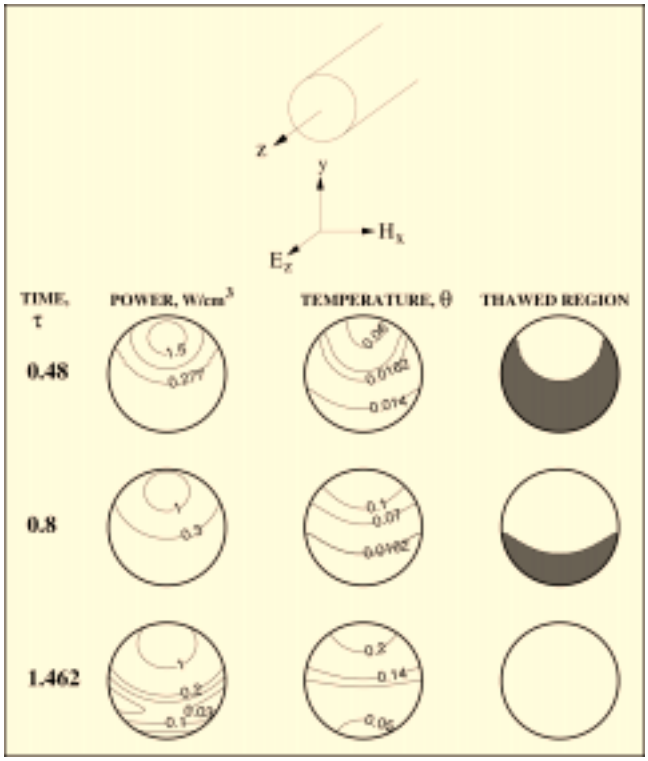

Figure 10. Power and temperature contours with the thawed region in the absence of convection during microwave thawing for a $D = 1$ cm cylinder exposed to microwaves from the bottom.

$D/D_p = 0.18$, $D/\lambda_m = 0.58$, $Pr = 0.5$, $G = 9$, $St_m = 6.8$, $Bi = 0.01$. The temporal changes in power and temperature are similar to the case with convection and bottom incidence (Figure 7).

at the lower half of the sample. Figure 8 is similar to Figure 7 with the MWs incident from the top of the sample. In contrast liquid regions form at the bottom of the sample. Due to the higher power absorption occurring at the bottom of the cylinder, convection is greater (larger numerical values of the stream function) here than in the bottom incidence case where the hotter fluid was at the top of the sample (Figure 7). Comparison of the temperatures in the liquid indicates that enhanced convection leads to more uniform temperatures in the liquid regions. The increased distribution of heat lowers the thawing time to $\tau = 1.158$. In contrast to the bottom heated case where four convection cells appear when the sample is totally thawed (Figure 7) two large convection cells extend across the sample for MWs incident from the top (Figure 8).

In order to investigate the effect of the oscillation at the interface between the liquid and mushy regions which are observed in Figures 7 and 8 we carried out a series of discretization tests. The results shown in Figure 7 were carried out for 12×12 elements. A comparison with 10×10 elements is shown in Figure 9. Although the oscillations which occur during the initial stages of thawing in the power contours are larger in magnitude for the coarser discretization (Figure 9), there is virtually no change in temperatures and stream function values. The total thawing time remains unaffected. Other discretization tests also indicate that small oscillations in power are smoothed out due to conduction and have little effect beyond a minimum refinement. Although a very fine mesh might remove these oscillations at a considerable increase in computer time, our studies indicate that an oscillation free power absorption is not necessary to capture converged results in temperature and stream functions. We further note that the oscillations are considerably reduced as thawing proceeds.

In order to study the importance of convection on the thawing dynamics we carried out a simulation when thawing occurs by conduction alone. In Figure 10 the parameters are similar to those of Figures 7 and 8; however, convection in the liquid is absent. Results are shown for MWs incident from the bottom. Since convection is absent, the direction of MWs has no effect. The temporal changes in power and temperature are similar to the case with convection and bottom incidence (Figure 7), indicating that convection in the liquid plays a small role due to the hot fluid forming in the upper portions of the sample. In contrast convection can have a strong effect when the hotter fluid is at the bottom of the sample (Figure 8), reducing the thawing time by about 30% and resulting in more uniform temperatures.

When the diameter of the sample is increased, some interesting dynamics occur. In Figure 11 (bottom incidence) the sample diameter $D = 2$ cm, and $D/D_p = 0.87$. In contrast to the previous cases, thawing is seen to occur from both the upper and lower portions of the sample. The maximum in

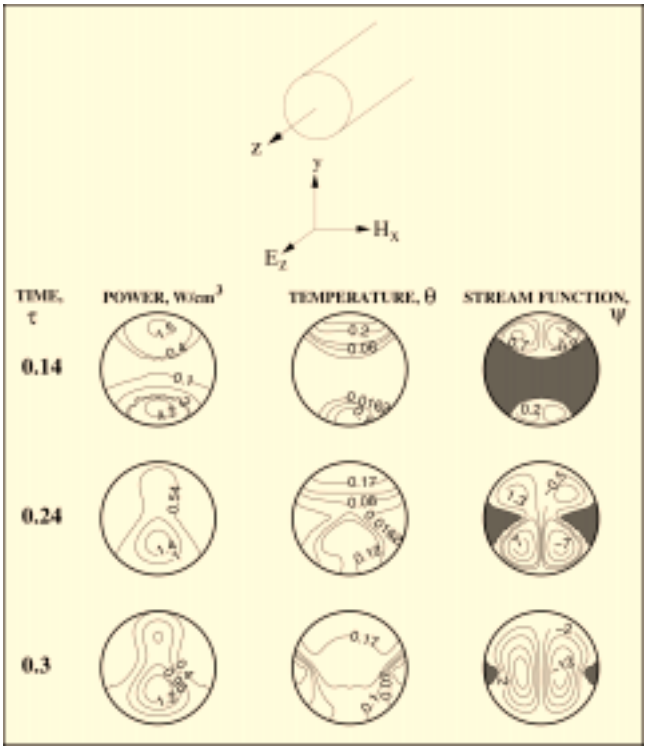

Figure 11. Power, temperature and stream function contours during microwave thawing for a D = 2 cm cylinder exposed to microwaves from the bottom.

$D/D_p = 0.87$, $D/\lambda_m = 0.98$, $Pr = 0.5$, $Ra_m = 1.33416 \times 10^5$, $G = 9$, $St_m = 6.8$, $Bi = 0.02$. Strong convection occurs due to a power maxima at the bottom.

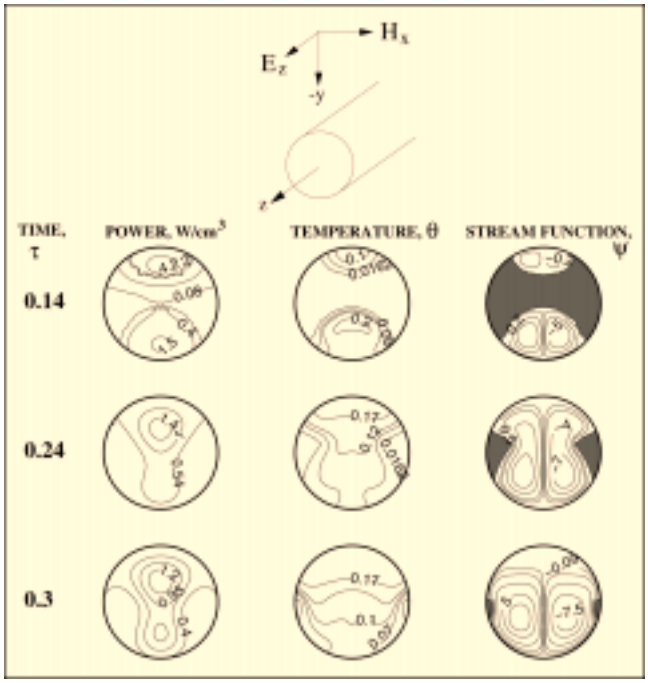

Figure 12. Same parameters as in Figure 11, but MWs are incident from the top.

Convection is not drastically reduced when compared with Figure 11.

power appears at the incident face during the early stages of thawing, and thawing occurs from both the top and bottom faces. At $\tau = 0.24$, the liquid regions extend across the samples with two mushy regions on opposite faces as seen in Figure 11. This situation gives rise to a cusp between the liquid and mushy regions. Convection is strong in this case due to the presence of the power maximum at the bottom. The opposite effect occurs when MWs are incident from the top (Figure 12). Since the maximum in power is located only in a small region at the top of the sample, convection is not drastically reduced when compared with Figure 11. Figure 13 illustrates the situation in the absence of convective effects in the liquid region. Although there is an increased rate of thawing during the initial stages ($\tau = 0.14$), the rate at which liquid region forms is very similar. The absence of convection during the early stages of thawing leads to an increase in the temperatures of the liquid regions and enhances the thawing during the early stages.

Figure 14 illustrates thawing in a sample where the $D/D_p = 3.73$ for $D = 2$ cm. This is the largest D/D_p ratio investigated. When MWs are incident from the bottom, liquid regions first form at the top face of the sample. In addition, a circular pocket of liquid appears in the lower portions of the sample. As thawing proceeds, the disconnected liquid regions merge, leaving two unthawed regions as seen $\tau = 0.2$. The effect of the larger D/D_p ratio is seen only during the final stages of thawing when the power absorption decays from the incident face. Since the hotter regions are at the bottom of the sample, convection is strong and the temperatures in the fluid are quite uniform. When MWs are incident from the top (Figure 15), the formation of liquid regions is similar in nature (but inverted). The main difference with the bottom incident case occurs during the late stages of thawing, where considerable stratification in temperature is observed due to the hotter fluid being in the upper regions of the sample. Convection plays a smaller role as seen by the lower values for the stream functions at $\tau = 0.3$. When convection is absent in the liquid, the temperature distributions are very similar to those observed in the presence of convection during the early and intermediate stages of thawing (Figures 14 and 16). During the final stages of thawing the stratification in temperatures is similar to that observed in Figure 15 (top incident) where convection is suppressed.

Figure 17 illustrates the average power and temperature profiles for $D = 1$ cm and $D = 2$ cm samples. In all cases there is an increase in absorbed power during the initial stages of thawing. The invariance of the average temperature for different cases is expected due to the small heat loss at the boundaries.

Discussion

Our results indicate that, when $D/D_p \ll 1$, the MW power absorption is uniform and thawing occurs uniformly across the sample, and, at the final stages of thawing, the entire region transforms to a liquid. Due to the unformity of power absorption at these length scales, both the direction of MWs

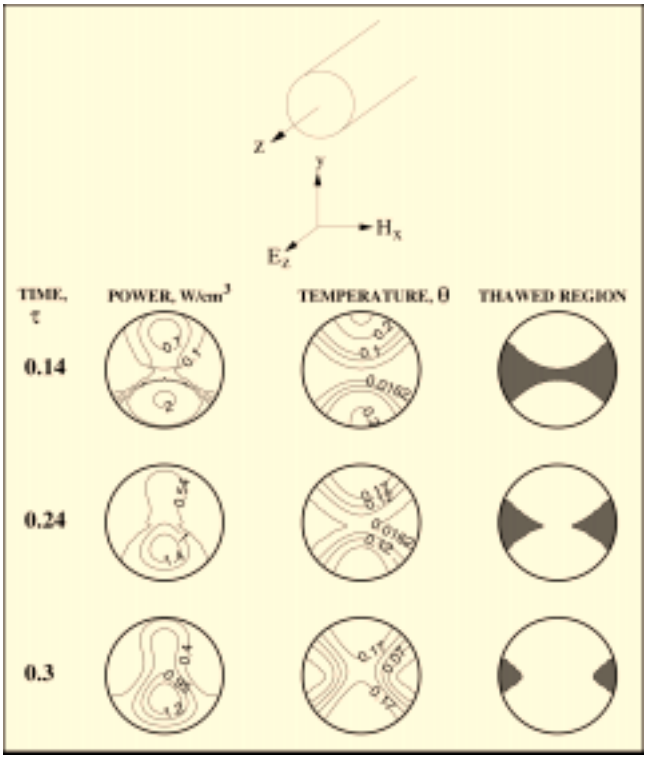

Figure 13. Power and temperature contours with the thawed region in the absence of convection, during microwave thawing of $D = 2$ cm cylinder exposed to microwaves from the bottom.

$D/D_p = 0.87$, $D/\lambda_m = 0.98$, $Pr = 0.5$, $G = 9$, $St_m = 6.8$, $Bi = 0.02$. The absence of convection leads to higher temperature in the liquid region during the earlier stages.

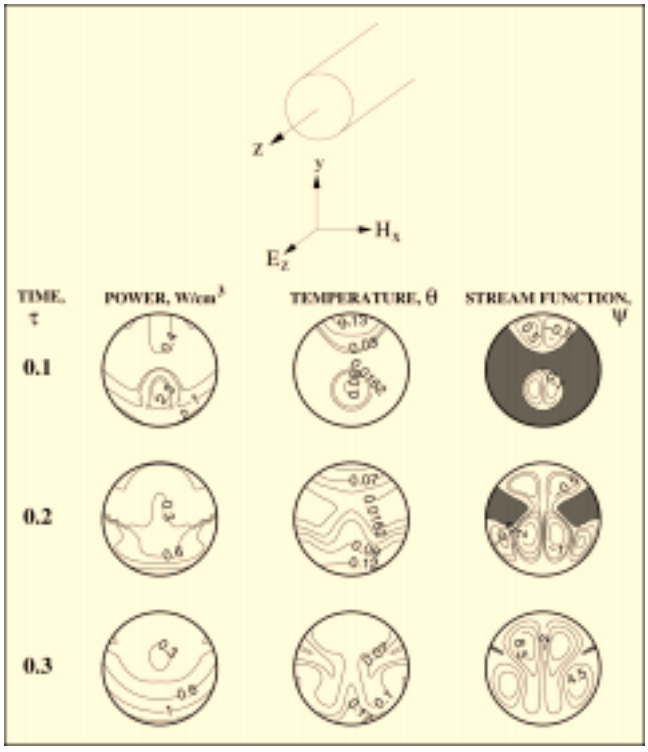

Figure 14. Power, temperature, and stream function contours during microwave thawing for a $D = 2$ cm cylinder exposed to microwaves from the bottom.

$D/D_p = 3.73$, $D/\lambda_m = 1.58$, $Pr = 0.5$, $Ra_m = 1.33416 \times 10^5$, $G = 9$, $St_m = 6.8$, $Bi = 0.02$. Strong convection leads to uniform temperature profiles.

and convection are seen to play a small role. At intermediate values of D/D_p, thawing is found to occur from the face opposite to the MWs or from both faces depending on the dielectric properties of the material. When $D/D_p \approx 1$ and a maximum in power occurs at the face opposite the incident face, the directionality of MWs plays an important role. Convection can transfer heat more efficiently when the hot fluid is at the bottom of the cylinder leading to a decrease in thawing times. These features are observed in Figures 7 and 8. The effect of the orientation of MWs on the convection and internal temperatures are similar to those observed by Ayappa et al. (1994) in their MW driven liquid convection studies, where strong convection and uniform heating was found for samples where the maximum power absorption occurred at the bottom of the sample.

In addition to a uniform power absorption, convection is also suppressed if multiply disconnected liquid regions form. Convection is reduced due to the smaller area available for flow in these regions. This is seen in Figures 11–13 where two disconnected liquid regions exist till the final stages of thawing for the $D = 2$ cm sample. Even though a strong maximum in power absorption occurs, convection plays a minor role here. This is clear on comparing the thawing times for bottom and top incidence (Figures 11–12). A similar pattern is observed in Figures 14–16 where $D/D_p \gg 1$. Here again two disconnected regions which form during the early stages of thawing considerably suppress convection. This is evident on examining the stream functions at $\tau = 0.2$ and 0.3 in Figure 14. Convection, however, does play a small role at the later stages of thawing for the bottom incident case where the power decays monotonically from the incident face (Figure 14). Convection helps in carrying heat away from the bottom and a smaller unthawed region is left, when compared with the top incident case where temperatures are stratified (Figure 15). Another point to note is the lower importance of convection during thawing in the larger sample, which have greater Rayleigh numbers, when compared with the smaller samples. This is primarily due to the presence of these disconnected liquid regions and smaller levels of power absorption.

The pattern of convection cell formation in the liquid phase deserves some mention. It is largely dictated by the power absorption and the topology of the unthawed regions. When the power maximum is at the top of the sample multiple cell (greater than two) formation is favored (Figures 7 and 15). This is also favored by the presence of local minima in the lower regions of the sample where the splitting in cells occurs (Figure 7). Uniform power absorption (Figures 5 and 6) or the presence of the power maximum at the bottom of the sample (Figures 8 and 11) lead to two large convection cells that extend across the sample. The presence of unthawed regions can give rise to secondary cells as seen in Figure 14 at the later stages of thawing.

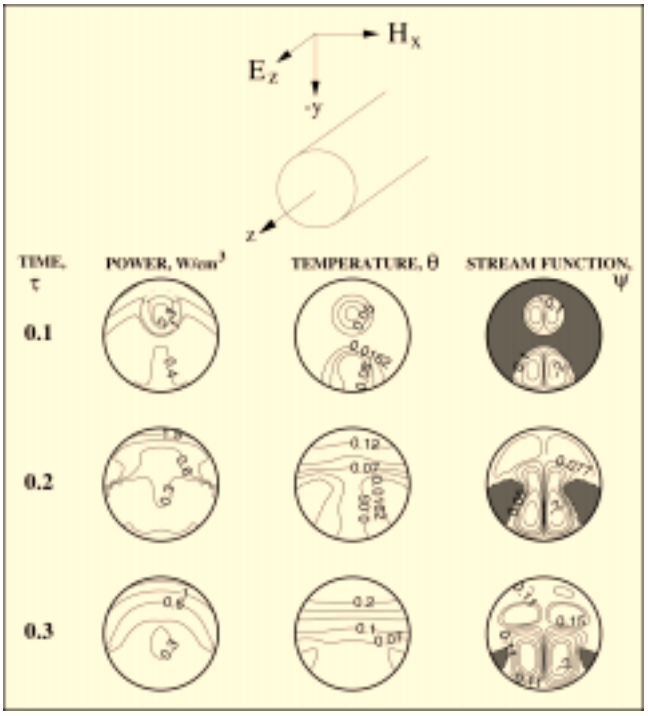

Figure 15. Same parameters as in Figure 14, but MWs are incident from the top.

In contrast with the bottom incident cylinder (Figure 14) stratification of temperature profiles are observed at the later stages of thawing and convection is suppressed.

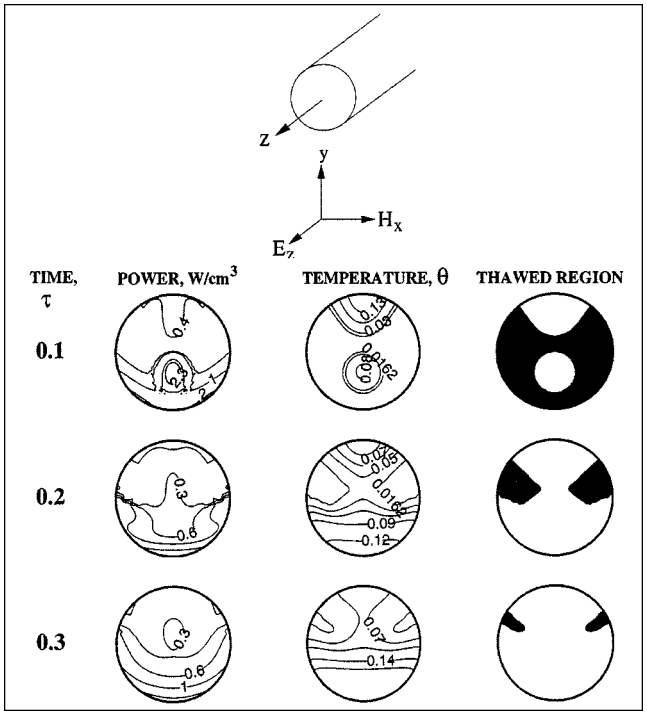

Figure 16. Power and temperature contours with the thawed region in the absence of convection, during microwave thawing for a $D = 2$ cm cylinder exposed to microwaves from the bottom.

$D/D_p = 3.73$, $D/\lambda_m = 1.58$; $Pr = 0.5$, $G = 9$, $St_m = 6.8$, $Bi = 0.02$. During the final stages of thawing the stratification in temperatures is similar to that observed in Figure 15 (top incidence) where convection is small.

Before concluding, we would like to discuss briefly the small oscillations observed in some cases during the early stages of thawing. The reasons for this feature could be attributed in part to the large gradients in power during the initial stages (Figure 17). It is well known that oscillations (Voller, 1996) in the front position are found to increase with a decrease in Stefan number ($St = C_0 \Delta T/\lambda$). In conventional melting studies the Stefan number is based on the temperature difference between the surface temperature and melting point. However, during MW thawing, this definition cannot be used. The St_m used in our work is based on a maximum allowable ΔT within the samples which may not reflect the true gradients. Consequently, the Stefan number (St) may be very low during the initial stages of thawing due to the small variation in temperature which could be responsible for the small oscillation observed. In addition to detailed convergence tests (discussed earlier) we find these oscillations are damped out as thawing proceeds (due to the increasing ΔT). Hence, we did not pursue this issue any further.

Conclusion

We have carried out extensive computations on 2-D MW thawing with internal convection of cylindrical samples with a distinct melting point. The enthalpy formulation with a superficial mushy region around the melting point efficiently captures multiple thawed domains that arise due to the penetration of MWs, permitting the computations to be carried out on a fixed mesh. All computations were carried out for a low dielectric loss, solid or frozen phase. A wide spectrum of thawing scenarios was investigated by varying the liquid-phase dielectric properties and sample diameters. Consequently, thawing was contrasted between samples where $0.032 < D/D_p < 3.73$ and $0.10 < D/\lambda_m < 1.58$. These ratios are computed based on the liquid phase D_p and λ_m. In all cases $Pr = 0.5$ and the Rayleigh number varied from 1.067×10^3 for the smallest diameter to 1.33416×10^5 in the largest sample studied ($D = 2$ cm). Thawing was contrasted for MWs being incident from the top and bottom faces of the cylinder and also with the thawing dynamics in the absence of convection in the liquid.

Our simulations indicate that for small sample diameters where $D/D_p \ll 1$, convection plays a small role and thawing is independent of the direction of MWs. At intermediate values of D/D_p where a strong maximum occurs in the power, convection plays an important role. If the power maximum is located at the bottom of the sample (depending on the orientation of MWs), convection is favored, heat is transported more effectively, and the thawing time is reduced. In contrast when the power maximum is at the top of the sample, the temperature gradients are increased. The position of the power maximum also dictates the pattern of convection cell formation. Multiple cells are favored when the power maximum is at the top of the sample or when unthawed regions

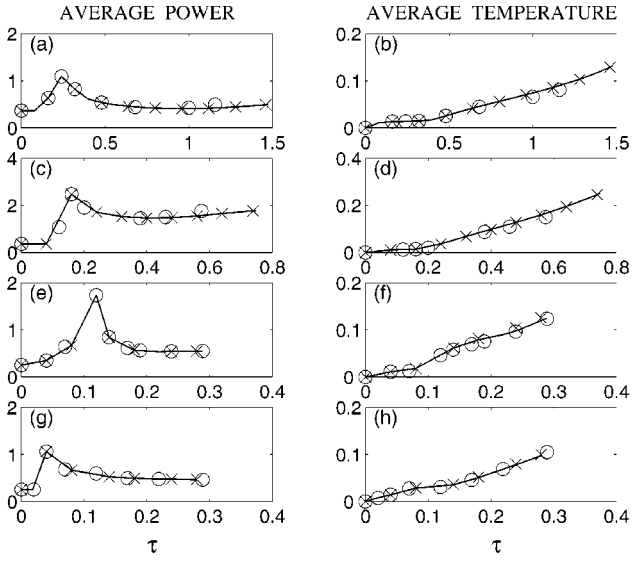

Figure 17. Average power ($W \cdot cm^{-3}$) and temperature profiles (θ) for various cases.

—, bottom incident; ○, top incident; ×, in the absence of convection. (a), (b) $D = 1$ cm, $D/D_p = 0.18$, $D/\lambda_m = 0.58$; (c), (d) $D = 1$ cm, $D/D_p = 1.26$, $D/\lambda_m = 0.67$; (e), (f) $D = 2$ cm, $D/D_p = 0.87$, $D/\lambda_m = 0.98$; (g), (h) $D = 2$ cm, $D/D_p = 3.73$, $D/\lambda_m = 1.58$.

break up the primary cell formation into secondary cells. The topology of the unthawed regions is seen to influence convection. In the presence of multiply connected thawed regions convection is generally suppressed due to the small sizes of liquid subdomains.

Acknowledgments

We are grateful to Pradip Dutta, J. N. Reddy and Simon Brandon for several useful discussions while this work was being carried out.

Literature Cited

Abramowitz, M., and I. A. Stegun, *Handbook of Mathematical Functions*, 9th ed., Dover, New York (1970).

Ayappa, K. G., ''Modeling Transport Processes During Microwave Heating: A Review,'' *Rev. in Chem. Eng.*, **13**, 1 (1997).

Ayappa, K. G., S. Brandon, J. J. Derby, H. T. Davis, and E. A. Davis, ''Microwave Driven Convection in a Square Cavity,'' *AIChE J.*, **40**, 1268 (1994).

Ayappa, K. G., H. T. Davis, E. A. Davis, and J. Gordon, ''Two-Dimensional Finite Element Analysis of Microwave Heating,'' *AIChE J.*, **38**, 1577 (1992).

Ayappa, K. G., H. T. Davis, E. A. Davis, and J. Gordon, ''Analysis of Microwave Heating of Materials with Temperature-Dependent Properties,'' *AIChE J.*, **37**, 313 (1991).

Basak, T., and K. G. Ayappa, ''Analysis of Microwave Thawing of Slabs with Effective Heat Capacity Method,'' *AIChE J.*, **43**, 1662 (1997a).

Basak, T., and K. G. Ayappa, ''Analysis of Microwave Thawing with the Effective Heat Capacity Method,'' *Proc. of Third ISHMT-ASME Heat and Mass Transfer Conf., and Fourteenth National Heat and Mass Transfer Conf.*, 289 (1997b).

Basak, T., K. K. Rao, and A. Bejan, ''A Model for Heat Transfer in a Honey Bee Swarm,'' *Chem. Eng. Sci.*, **51**, 387 (1996).

Batchelor, G. K., *An Introduction to Fluid Dynamics*, Cambridge University Press, Cambridge, U.K. (1993).

Brent, A. D., V. R. Voller, and K. J. Reid, ''Enthalpy-Porosity Technique for Modeling Convection-Diffusion Phase Change: Application to the Melting of a Pure Metal,'' *Numer. Heat Transfer*, **13**, 297 (1988).

Dalhuijsen, A. J., and A. Segal, ''Comparison of Finite Element Techniques for Solidification Problems,'' *Int. J. Num. Methods in Eng.*, **23**, 1807 (1986).

Dantzig, J. A., ''Modeling Liquid-Solid Phase Changes with Melt Convection,'' *Int. J. Num. Methods in Eng.*, **28**, 1769 (1989).

Datta, A., H. Prosteya, and W. Hu, ''Mathematical Modeling of Batch Heating of Liquids in a Microwave Cavity,'' *J. Microwave Power and EM Eng.*, **27**, 38 (1992).

Datta, A., H. Prosteya and W. Hu, ''Batch Microwave Heating of Liquids: An Experimental Study,'' *J. Microwave Power and EM Eng.*, **26**, 215 (1991).

Dutta, P., Y. Joshi, and R. Janaswami, ''Thermal Modeling of Gas Tungsten Arc Welding Process with Nonaxisymmetric Boundary Conditions,'' *Numer. Heat Transfer*, A, **27**, 499 (1995).

Gartling, D. K., ''A Finite Element Analysis of Volumetrically Heated Fluids in an Axisymmetric Enclosure,'' in *Finite Element in Fluids*, **4**, R. H. Gallagher, D. N. Norrie, J. T. Oden, and O. C. Zienkiewicz, eds., Wiley, New York (1982).

Gau, C., and R. Viskanta, ''Melting and Solidification of a Pure Metal on a Vertical Wall,'' *Int. J. Heat Mass Transfer*, **108**, 174 (1986).

Gilchrist, J., G. A. Kreigsmann, and D. T. Papageorgiou, ''Stability of a Microwave Heated Fluid Layer,'' *IMA J. Appl. Math.*, **60**, 73 (1998).

Hughes, T.J. R., W. K. Liu, and A. Brooks, ''Finite Element Analysis of Incompressible Viscous Flows by the Penalty Function Formulation,'' *J. Comp. Phys.*, **30**, 1 (1979).

Kuehn, T. H., and R. J. Goldstein, ''An Experimental and Theoretical Study of Natural Convection in the Annulus between Horizontal Concentric Cylinders,'' *J. Fluid Mech.*, **74**, 695 (1976).

Mallinson, G. D., and G. D. vahl Davis, ''Three-Dimensional Natural Convection in a Box: A Numerical Study,'' *J. Fluid Mech.*, **83**, 1 (1977).

Nield, D., and A. Bejan, *Convection in Porous Media*, Second Edition, Springer, New York (1998).

Pangrle, B. P., K. G. Ayappa, H. T. Davis, E. A. Davis, and J. Gordon, ''Microwave Thawing of Cylinders,'' *AIChE J.*, **37**, 1789 (1991).

Pangrle, B. P., K. G. Ayappa, E. Sutanto, H. T. Davis, E. A. Davis, and J. Gordon, ''Microwave Thawing of Lossy Dielectric Materials,'' *Chem. Eng. Comm.*, **112**, 39 (1992).

Patankar, S. V. *Numerical Heat Transfer and Fluid Flow*, Hemisphere Washington, DC (1980).

Reddy, J. N., *An Introduction to the Finite Element Method*, McGraw-Hill, New York (1993).

Schreiber, R., and H. B. Keller, ''Driven Cavity Flows by Efficient Numerical Techniques,'' *J. Comp. Phys.*, **49**, 310 (1983).

Talmon, Y., H. T. Davis, and L. E. Scriven, ''Moving Boundary Problems in Simple Shapes Solved by Isotherm Migration,'' *AIChE J.*, **29**, 795 (1983).

Voller, V. R., and C. Prakash, ''A Fixed Grid Numerical Modelling Methodology for Convection-Diffusion Mushy Region Phase-Change Problems,'' *Int. J. Heat Mass Transfer*, **30**, 1709 (1987).

Voller, V. R., ''An Overview of Numerical Methods for Solving Phase Change Problems,'' *Advances in Num. Heat Transfer*, **1** (1996).

Appendix A

An estimate of the relative importance of internal convection and conduction (Basak et al., 1996) may be obtained by treating the mushy region as a porous medium in a cylinder of diameter D. The rate of heat transfer per unit volume of the cylinder by convection within the cylinder may be estimated as

$$H_{\text{conv}} \sim C_{\text{eff}}\left(u\frac{\Delta T}{D}\right), \tag{A1}$$

where C_{eff} is the effective heat capacity of the mushy region, u is the characteristic velocity due to free convection, and ΔT is the characteristic temperature difference within the mushy region. An estimate of u may be obtained from the y component momentum balance (Nield and Bejan, 1998)

$$-\frac{\partial p}{\partial y}-\frac{\mu}{K}u-\rho_0(1-\beta\Delta T)g=0, \tag{A2}$$

where p is the pressure, ρ_0 is the reference density of the liquid in the mushy region, μ is the viscosity of the liquid in the mushy region, K is the permeability of the mushy region, β is the volume expansion coefficient, and g is the acceleration due to gravity. Setting $p=p_0+p'$, where p' is the dynamic pressure, the static pressure p_0 satisfies

$$\frac{\partial p_0}{\partial y}=-\rho_0 g.$$

Hence, the y component momentum balance is

$$-\frac{\partial p'}{\partial y}-\frac{\mu}{K}u+\rho_0\beta\Delta Tg=0. \tag{A3}$$

Since the flow is driven by buoyancy, the contribution from pressure driven flow is small, and an estimate of the characteristic velocity obtained by balancing viscous and body force terms in Eq. A3 is

$$u\sim u_y\sim\frac{K\rho_0\beta\Delta Tg}{\mu}. \tag{A4}$$

The rate of heat transfer per unit volume of the mushy region by conduction may be estimated as

$$H_{\text{cond}}\sim k_{\text{eff}}\left(\frac{\Delta T}{D^2}\right). \tag{A5}$$

Hence, the ratio of heat transfer by convection and conduction obtained from Eqs. A1, A4 and A5 is

$$\frac{H_{\text{conv}}}{H_{\text{cond}}}\sim Ra_p\equiv\frac{C_{\text{eff}}K\rho_0\beta g\Delta TD}{k_{\text{eff}}\mu}, \tag{A6}$$

where Ra_p is the Rayleigh number for the porous medium. For a porous medium composed of spheres of diameter d_p, the permeability estimated using the Carman-Kozeny equation (Nield and Bejan, 1998) is

$$K=\frac{d_p^2\epsilon^3}{180(1-\epsilon)^2}, \tag{A7}$$

where ϵ is the porosity.

The parameters in Eq. A6 are estimated in SI units as follows. If d_p is $O(10^{-2})$, $\epsilon=0.5$, then $K=2.8\times10^{-7}$. With $C_{\text{eff}}=O(10^3)$, $\rho_0=O(10^3)$, $\beta=O(10^{-4})$, $g=O(10)$, $\Delta T=0.2$, $D=0.02$, $k_{\text{eff}}=O(1)$ and $\mu=O(5\times10^{-4})$, $H_{\text{conv}}/H_{\text{cond}}\sim2.22\times10^{-3}$.

Appendix B

This section discusses the procedure used to evaluate the RBC within the boundary integrals (the last terms of Eqs. 35 and 36) for a half domain as shown in Figure 3. The first terms in Eqs. 21 and 22 within the boundary integral are evaluated over all the elements in the half domain. In contrast, the second and third terms of Eqs. 21 and 22 include the product of boundary integrals for the half as well as the full domain. We outline the derivation only for the second term of Eq. 21. A similar approach is used for the other terms in the RBC which involve double integrals. Consider the half domain consisting of M nodes on Γ_2 (see Figure 3) which implies a total of $2M-2$ electric field (v_z,w_z) unknowns for the full domain. Expanding the second term of Eq. 21, and incorporating the expansion Eq. 34 for v_z, we get

$$\sum_{n=0}^{\infty}Re(D_n)[I_{11}I_{12}+I_{21}I_{22}] \tag{B1}$$

where

$$I_{11}=\int_{\Gamma_2}\Phi_i(\phi)\cos n\phi\ d\phi,$$

$$I_{12}=\sum_{j=1}^{2M-2}v_{z,j}\int_0^{2\pi}\Phi_j(\phi')\cos n\phi' d\phi',$$

$$I_{21}=\int_{\Gamma_2}\Phi_i(\phi)\sin n\phi d\phi,$$

$$I_{22}=\sum_{j=1}^{2M-2}v_{z,j}\int_0^{2\pi}\Phi_j(\phi')\sin n\phi' d\phi'. \tag{B2}$$

The integrals I_{11} and I_{21} are evaluated over all the elements on Γ_2. To evaluate I_{12} and I_{22}, we exploit the reflective symmetry for the v_js since we are only interested in the solution on Γ_2. Noting that for a given node $1<j<M$ on Γ_2, the equivalent reflected node is $2M-j$,

$$\begin{aligned}I_{12}&=\sum_{j=1}^{M}v_{z,j}\int_0^{2\pi}\Phi_j(\phi')\cos n\phi' d\phi'\\&\quad+\sum_{j=M+1}^{2M-2}v_{z,j}\int_0^{2\pi}\Phi_j(\phi')\cos n\phi' d\phi'\\&=\sum_{j=1}^{M}v_{z,j}\int_0^{2\pi}\Phi_j(\phi')\cos n\phi' d\phi'\\&\quad+\sum_{j=2}^{M-1}v_{z,j}\int_0^{2\pi}\Phi_{2M-j}(\phi')\,n\phi' d\phi'\\&=\sum_{j=1}^{M}v_{z,j}\Bigg[\int_0^{2\pi}\Phi_j(\phi')\cos n\phi' d\phi'\\&\qquad+\beta_{1j}\beta_{Mj}\int_0^{2\pi}\Phi_{2M-j}(\phi')\cos n\phi' d\phi'\Bigg].\end{aligned}$$

I_{22} can be evaluated in a similar manner. The final form of the second term in Eq. 46 is thus obtained with the substitution of I_{11}, I_{12}, I_{21} and I_{22} into Eq. B1.

Manuscript received Oct. 1, 1999, and revision received Sept. 15, 2000.